

Orbital torque switching of room temperature two-dimensional van der Waals ferromagnet Fe₃GaTe₂

Delin Zhang^{1,2,3,†,*}, Heshuang Wei^{1,†}, Jinyu Duan^{1,†}, Jiali Chen^{4,†}, Dongdong Yue⁵, Yuhe Yang², Jinlong Gou¹, Junxin Yan⁵, Kun Zhai⁵, Ping Wang¹, Shuai Hu¹, Zhiyan Jia², Wei Jiang^{4,*}, Wenhong Wang^{1,2,3}, Yue Li³, Yong Jiang^{1,2,3,*}

1. Institute of Quantum Materials and Devices; School of Electronic and Information Engineering, Tiangong University, Tianjin, 300387, China.
2. School of Material Science and Engineering; State Key Laboratory of Separation Membrane and Membrane Processes, Tiangong University, Tianjin, 300387, China.
3. School of Physical Science & Technology, Tiangong University, Tianjin, 300387, China.
4. Centre for Quantum Physics, Key Laboratory of Advanced Optoelectronic Quantum Architecture and Measurement (MOE); Beijing Key Lab of Nanophotonics & Ultrafine Optoelectronic Systems, School of Physics, Beijing Institute of Technology, Beijing, 100081, China.
5. Center for High Pressure Science, State Key Laboratory of Metastable Materials Science and Technology, Yanshan University, Qinhuangdao 066000, China

†These authors contributed equally: Delin Zhang, Heshuang Wei, Jinyu Duan, Jiali Chen

*Corresponding authors. Email: zhangdelin@tiangong.edu.cn (D.L.Z.), wjiang@bit.edu.cn (W.J.) and yjiang@tiangong.edu.cn (Y.J.)

Abstract

Efficiently manipulating the magnetization of van der Waals (vdW) ferromagnets has attracted considerable interest in developing room-temperature two-dimensional (2D) material-based memory and logic devices. Here, taking advantage of the unique properties of the vdW ferromagnet as well as promising characteristics of the orbital Hall effect, we demonstrate the room-temperature magnetization switching of vdW ferromagnet Fe₃GaTe₂ through the orbital torque generated by the orbital Hall material, Titanium (Ti). The switching current density is estimated to be around 1.6×10^6 A/cm², comparable to that achieved in Fe₃GaTe₂ using spin-orbit torque from spin Hall materials (e.g., WTe₂, and TaIrTe₄). The efficient magnetization switching arises from the combined effects of the large orbital Hall conductivity of Ti and the strong spin-orbit correlation of the Fe₃GaTe₂, as confirmed through theoretical calculations. Our findings advance the understanding of orbital torque switching and pave the way for exploring 2D material-based orbitronic devices.

Spintronic devices have been extensively studied for their potential in developing energy-efficient memory and computing components, offering ultrahigh storage density, ultrafast switching speed, ultralow energy consumption, and excellent scalability (1-3). These devices are primarily manipulated through spin-transfer torque (STT), where the charge current can be converted into spin current via the ferromagnets with high spin polarization (4), or by spin-orbit torque (SOT), where the conversion happens through spin Hall materials (SHMs) with strong spin-orbit coupling (SOC) (5-7). Despite significant advancements over the past decade, spintronic memory devices still face several challenges. STT-based memory devices struggle with relatively low endurance, high switching current density, and Joule heating caused by current flowing through the tunnel barrier. SOT-based devices require SHMs with strong SOC for efficient spin-torque generation. Recently, attention has increasingly shifted toward orbitronic devices, where device manipulation is driven by orbital torque (OT) generated by the orbital Hall effect (OHE) through an orbital Hall material (OHM) with the weak SOC (8-22). This approach has the potential to overcome the challenges faced by spintronic devices.

The OHE originates from the orbital texture created by orbital hybridization, which generates finite orbital angular momentum along the direction of $\mathbf{E} \times \mathbf{k}$ under an external electric field (\mathbf{E}) (8-10). Unlike STT (4) and SOT devices, which rely solely on charge-to-spin conversion (5-7), OT devices involve two stages of current conversion: the charge-to-orbital current conversion in the OHM and the orbital-to-spin current conversion in the adjacent ferromagnetic (FM) material. This

unique mechanism allows for tuning the OT efficiency (ζ_{OT}) by designing novel heterostructures with optimal selections of OHM and FM material combinations (20). So far, many OHMs have been predicted to efficiently convert charge current to orbital current due to their giant orbital Hall conductivity (σ_{OHE}) (9,11,16). Experiments have shown these materials have a large ζ_{OT} (~ 0.78) (20) and a long orbital diffusion length (λ_{OHE}) (~ 60 nm) (16). However, the options for FM materials capable of efficiently converting orbital current to spin current are limited, particularly for perpendicular magnetic anisotropy (PMA) materials with a strong spin-orbit correlation (15,20,23). Therefore, exploring novel PMA FM materials is crucial for advancing orbitronic devices.

Recent advancements in two-dimensional van der Waals (2D-vdW) materials have led to the experimental confirmation of various 2D-vdW magnetic materials, opening new avenues for innovative room-temperature 2D-vdW spintronic technologies (24-27). Among these advancements, 2D-vdW Fe_3GaTe_2 has emerged as a particularly promising FM material, drawing considerable attention for its potential applications in tunnel magnetoresistance (28,29), magnetic skyrmions (30-33), and SOT devices (34-39). This interest is driven by its clean surface, large PMA ($K_{\text{u}} > 3.88 \times 10^5 \text{ J/m}^3$), and high Curie temperature ($T_{\text{c}} > 350 \text{ K}$) (40). Notably, SOT-driven magnetization switching in Fe_3GaTe_2 -based heterostructures has been experimentally demonstrated using SHMs with large SOC, such as heavy metals (34-36), topological insulators (37), and topological semimetals (38,39). However, the OT-driven magnetization switching of the Fe_3GaTe_2 layer has yet to be observed, and the

underlying switching mechanism for 2D-vdW ferromagnets remains elusive.

In this work, we experimentally investigated the OT-driven magnetization switching of the 2D-vdW ferromagnet Fe_3GaTe_2 through the Ti OHM and provided a theoretical understanding of the OT-driven magnetization switching mechanism. The Fe_3GaTe_2 -based heterostructures were fabricated and patterned into Hall bar devices, followed by measuring the current-induced magnetization switching. We found that the Ti OHM enables switching of the Fe_3GaTe_2 layer at room temperature in the $\text{Fe}_3\text{GaTe}_2/\text{Ti}$ device with a significantly lower switching current density ($J_s \sim 1.6 \times 10^6 \text{ A/cm}^2$). Meanwhile, first-principles calculations were employed to analyze the spin-orbit correlation in Fe_3GaTe_2 structures, shedding light on the underlying mechanism of OT-driven magnetization switching of 2D-vdW FM materials. These findings highlight the significance of spin-orbit correlation in the PMA FM layer, providing valuable insights for the design and development of 2D-vdW orbitronic devices.

Discussion and results

Orbital Torque Device Based on 2D-vdW Ferromagnet

In 2D-vdW FM SOT heterostructures, spin currents can be generated by SHMs [e.g., Pt (34-36), $\text{Bi}_{1.1}\text{Sb}_{0.9}\text{Te}_2\text{S}_1$ (37), and WTe_2 (39)], and then these spin currents flow into 2D-vdW ferromagnets, exerting a torque that switches their magnetization. The efficiency of the magnetization switching mainly depends on the spin Hall angle (θ_{SHE}) of the SHMs. On the other hand, in 2D-vdW FM OT heterostructures, the switching efficiency depends not only on the orbital Hall angle (θ_{OHE}) of the OHMs

but also on the orbital-to-spin conversion coefficient (η_{L-S}) of the 2D-vdW ferromagnets. OHMs with high σ_{OHE} convert charge current into orbital current via the OHE. The orbital current then flows into the adjacent 2D-vdW FM layer, where it is converted into spin current through strong spin-orbit correlation, generating the torque to switch the magnetization of the 2D-vdW FM layer, as shown in the left panel of Fig. 1a. Therefore, both OHMs with high σ_{OHE} and 2D-vdW FM materials with strong spin-orbit correlation are essential for enhancing the ζ_{OT} .

Here, we selected Ti as the OHM and the 2D-vdW Fe_3GaTe_2 as the PMA FM layer to investigate the charge-to-orbital-to-spin current conversion and the OT-driven magnetization switching. The charge current can efficiently convert into the orbital current through the Ti OHM, which has a larger σ_{OHE} , calculated to be approximately $4600 (\hbar/e)(\text{S}/\text{cm})$. It is worth noting that, due to its weak SOC, Ti exhibits a negligible spin Hall conductivity (σ_{SHE}) of only about $11 (\hbar/e)(\text{S}/\text{cm})$, effectively ruling out the possibility of any significant SOT effect, as shown in Fig. 1b (16). The orbital currents generated in the Ti OHM layer can be efficiently converted into spin currents due to the strong SOC in the Fe_3GaTe_2 layer (see the right panel of Fig. 1a).

The Fe_3GaTe_2 possesses the hexagonal lattice structure with two adjacent quintuple-layered substructures separated by a vdW gap, where each quintuple layer consists of a Fe_3Ga heterometallic slab sandwiched between two Te layers, as illustrated in Fig. 1a. Fe_3GaTe_2 single crystal samples, grown by the self-flux method, exhibit high-quality crystallinity, as demonstrated by prominent $(00L)$ Bragg peaks (see Supplementary Fig. 1a) with an estimated Curie temperature of ~ 365 K (see

Supplementary Fig. 1b and Supplementary Note 1 for more details). Figure 1c presents the anomalous Hall resistance (R_{AHE}) versus (vs.) out-of-plane external magnetic field (H_{ext}) as a function of temperature for the Fe_3GaTe_2 nanoflake. The square R_{xy} vs. H_{ext} loops affirm excellent PMA. Meanwhile, the single crystal feature and vdW layered structure were verified by atomic-resolution scanning transmission electron microscopy (STEM) measurements, as shown in Fig. 1d. These results verify that the Fe_3GaTe_2 single crystal samples are of high quality, making them suitable for investigating 2D-vdW ferromagnet OT heterostructures.

Orbital Torque Switching of 2D-vdW Ferromagnet

To experimentally investigate the OT-driven magnetization switching, we fabricated the 2D-vdW FM $\text{Fe}_3\text{GaTe}_2/\text{Ti}$ samples on the Si/SiO₂ substrates, which were patterned into Hall bar devices ($15\ \mu\text{m} \times 6\ \mu\text{m}$) (see the inset of Fig. 2a and Supplementary Fig. 2a) and characterized for current-induced magnetization switching through the OT (see the device fabrication and transport-property measurements in Methods). To assess the PMA of the Fe_3GaTe_2 (15.8 nm)/Ti (10.0 nm) Hall bar device, the room temperature R_{AHE} vs. H_{ext} loop was measured with the in-plane H_{ext} , as shown in Fig. 2a and Supplementary Fig. 2b. The effective anisotropy fields (H_{K}) were estimated to be 4.02 T ~ 5.33 T as the temperature decreased from 300 K to 225 K, verifying a very strong PMA (36,38,39). Meanwhile, the R_{AHE} vs. H_{ext} loops at even lower temperatures were measured to further characterize the PMA, as plotted in Fig. 2b. The Hall bar device demonstrates 100% remanence with well-defined rectangle R_{AHE} vs. H_{ext} loops. The coercivity (H_{C}) of the

Fe₃GaTe₂ (15.8 nm)/Ti (10.0 nm) Hall bar device increases from 19 mT at 300 K to 540 mT at 10 K, indicating very strong PMA. In addition, as the device was cooled from 300 K to 225 K, the value of R_{xy} increases from 4.7 Ω to 7.7 Ω , as plotted in Fig. 2c, suggesting the excellent magnetic properties of the 2D-vdW Fe₃GaTe₂ layer.

To demonstrate the OT-driven magnetization switching of the 2D-vdW FM Fe₃GaTe₂ layer, the R_{AHE} vs. the pulse current (I_{pulse}) loops of the Fe₃GaTe₂ (15.8 nm)/Ti (10.0 nm) Hall bar device were measured with 1 ms write-pulse with a 6s delay followed by read pulses (± 1.0 mA) under in-plane $H_{\text{ext}} \sim \pm 20$ mT - ± 150 mT applied along the current direction (see details in Supplementary Note 2). The experimental results are shown in Fig. 2d and Supplementary Figs. 3-5. Although the Curie temperature of the Fe₃GaTe₂ single-crystal sample is around 365 K (see Supplementary Fig. 1b), it will be slightly lower for the 2D-vdW FM Fe₃GaTe₂ thin film (36). This will decrease the PMA when the I_{pulse} is applied during the measurement of current-induced magnetization switching. Consequently, R_{AHE} vs. I_{pulse} measurements were carried out at 300 K, 275 K, 250 K, and 225 K to ensure the FM state of Fe₃GaTe₂ with good PMA while studying the temperature-dependent magnetization switching behavior. Figure 2d presents the R_{AHE} vs. I_{pulse} loops of the Fe₃GaTe₂ (15.8 nm)/Ti (10.0 nm) Hall bar device measured with temperatures from 300 K to 225 K in the presence of a ± 100 mT in-plane H_{ext} . The low resistance and high resistance states were observed at the measured temperatures when switching the I_{pulse} from positive to negative polarities. Reversing the direction of the in-plane H_{ext} also resulted in a reversal of the polarity in the R_{AHE} vs. I_{pulse} loops. Meanwhile, the

ratio of magnetization switching exhibited an initial increase followed by a decrease as the in-plane H_{ext} increased, as shown in Supplementary Figs. 3-5. This behavior excludes thermal effects and confirms that the 180 °magnetization switching is driven by the OT from the Ti OHM. In addition, the R_{AHE} vs. I_{pulse} loops of the Fe_3GaTe_2 (15.8 nm)/Ti (10.0 nm) Hall bar device become rectangle (see Fig. 2c) as the measured temperature decreased from 300 K to 225 K, suggesting the complete magnetization switching. Figure 2e shows the switching current density (J_S) and switching ratio as functions of temperature for the Fe_3GaTe_2 (15.8 nm)/Ti (10.0 nm) Hall bar device. It can be observed that the J_S gradually increases from 1.6×10^6 A/cm² to 4.8×10^6 A/cm² as the temperature decreases, attributed to the enhanced magnetic properties (e.g. PMA) of the Fe_3GaTe_2 layer as the temperature decreases. Notably, we observed that the switching ratio also increases as the devices are cooled. This enhancement may be attributed to reduced thermal perturbation, which leads to improved interlayer coupling between vdW layers and better alignment of magnetic moments of the Fe_3GaTe_2 .

Orbital Torque vs. Spin-orbit Torque

To further investigate the torque efficiency of OT, SOT, and the combined SOT+OT, we designed and prepared two additional samples: the SOT sample Fe_3GaTe_2 (18.3 nm)/Pt (5.0 nm) and the SOT+OT sample Fe_3GaTe_2 (16.7 nm)/Pt (2.0 nm)/Ti (10.0 nm). These samples were then patterned into the Hall bar devices (24 $\mu\text{m} \times 8 \mu\text{m}$), all of which exhibit excellent PMA properties, as evidenced by their square R_{AHE} vs. H_{ext} loops. Subsequently, current-induced orbital/spin torque

magnetization switching was performed under an in-plane H_{ext} applied along the current direction (see Fig. 3, Supplementary Note 2, and Supplementary Figs. 6-9). Unlike the squared R_{AHE} vs. H_{ext} loops, the R_{AHE} vs. J_{S} loops do not always exhibit a perfectly squared signal measured at room temperature due to the thermal effect which resulted in magnetic moment disarrangement and PMA decrease. To ensure a fair comparison between different devices, we selected the R_{AHE} vs. J_{S} loops measured at 275 K under an in-plane $H_{\text{ext}} = 100$ mT, where all devices display near square-shaped R_{AHE} vs. J_{S} loops. We note that the slight variation in Fe_3GaTe_2 thickness across different devices does not significantly affect J_{S} , as confirmed by our test measurements with various thicknesses. Figures 3a-3c present the R_{AHE} vs. J_{S} loops measured at 275K of Fe_3GaTe_2 (15.8 nm)/Ti (10.0 nm), Fe_3GaTe_2 (16.7 nm)/Pt (2.0 nm)/Ti (10.0 nm), and Fe_3GaTe_2 (18.3 nm)/Pt (5.0 nm) Hall bar devices. Deterministic magnetization switching was observed in all devices, with J_{S} estimated to be approximately 2.4×10^6 A/cm², 5.9×10^6 A/cm², and 9.2×10^6 A/cm² for the respective devices. Notably, the J_{S} of the Fe_3GaTe_2 (15.8 nm)/Ti (10.0 nm) device is about four times smaller than that of the Fe_3GaTe_2 (18.3 nm)/Pt (5.0 nm) device, suggesting that the OT efficiency in the $\text{Fe}_3\text{GaTe}_2/\text{Ti}$ heterostructure is higher than the SOT efficiency in the $\text{Fe}_3\text{GaTe}_2/\text{Pt}$ heterostructure. For the combined OT and SOT effect, the J_{S} (5.9×10^6 A/cm²) is higher than in the OT-only $\text{Fe}_3\text{GaTe}_2/\text{Ti}$ device but lower than in the SOT-only $\text{Fe}_3\text{GaTe}_2/\text{Pt}$ device.

Figure 3d illustrates the possible physical mechanism behind the magnetization switching of these devices with different switching efficiency. For the $\text{Fe}_3\text{GaTe}_2/\text{Pt}$

device, the charge current directly converts into the spin current in the Pt layer, the switching efficiency mainly depends on the SOT from the Pt SHM ($\sigma_{\text{SHE,Pt}}$), as shown in the left panel of Fig. 3d. However, for the $\text{Fe}_3\text{GaTe}_2/\text{Ti}$ device, the switching efficiency is primarily influenced by both the OT of the Ti OHM ($\sigma_{\text{OHE,Ti}}$) and the spin-orbital correlation strength of the 2D-vdW FM Fe_3GaTe_2 layer. The charge current first converts into the orbital current in the Ti layer and then the orbital current is converted into the spin current via the 2D-vdW FM Fe_3GaTe_2 layer, as presented in the right panel of Fig. 3. Considering the large OHE of the Ti, the significantly lower J_S of the $\text{Fe}_3\text{GaTe}_2/\text{Ti}$ device compared to that of the $\text{Fe}_3\text{GaTe}_2/\text{Pt}$ device indicates a rather strong spin-orbit correlation within the 2D-vdW FM Fe_3GaTe_2 layer. For the $\text{Fe}_3\text{GaTe}_2/\text{Pt}/\text{Ti}$ device, the Pt SHM serves as an SOT source, and the Ti OHM acts as an OT source. The spin current originates from two mechanisms: the charge-to-spin current conversion through the Pt SHM and the charge-to-orbital-to-spin current conversion through the Ti OHM and the 2D-vdW FM Fe_3GaTe_2 layer. During this process, the Pt SHM converts not only the charge current into the spin current but also some of the orbital current from the Ti OHM into the spin current (41,42). The rest orbital current from the Ti OHM will pass through the Pt layer and flow into the 2D-vdW FM Fe_3GaTe_2 layer, and then be converted into spin current. The Pt layer may partially screen the orbital current flowing from the Ti OHM into the 2D-vdW FM Fe_3GaTe_2 layer, which diminishes the OT switching efficiency compared to that of the pure OT device, $\text{Fe}_3\text{GaTe}_2/\text{Ti}$. As a result, the J_S ($\sim 5.9 \times 10^6 \text{ A/cm}^2$) of the $\text{Fe}_3\text{GaTe}_2/\text{Pt}/\text{Ti}$ device falls between the values observed for the $\text{Fe}_3\text{GaTe}_2/\text{Ti}$ and the

Fe₃GaTe₂/Pt devices. We also summarize the J_S as a function of the in-plane H_{ext} for the 2D-vdW FM Fe₃GaTe₂ devices measured at room temperature switched by the different SHMs and OHMs, as plotted in Fig. 3e. Very interestingly, the J_S of the Fe₃GaTe₂ devices switched via the light material Ti through OT is comparable to that of the Fe₃GaTe₂ devices driven by topological quantum materials through SOT [e.g. Bi_{1.1}Sb_{0.9}Te₂S₁ (37), TaIrTe₄ (38), and WTe₂ (39)]. This finding highlights the highly efficient conversion process of charge-to-orbital-to-spin currents in the 2D-vdW FM Fe₃GaTe₂ layer, with potential implications for other 2D-vdW ferromagnets.

Spin-orbit Correlation in the vdW ferromagnet

Based on the experimental results, we demonstrated that the Fe₃GaTe₂/Ti device exhibits high OT efficiency, as evidenced by its low J_S , which arises from the contribution of both the Ti OHM and the 2D-vdW FM Fe₃GaTe₂ layer. The σ_{OHE} of the Ti OHM has been calculated to be ~ 4600 (\hbar/e)(S/cm) (see Fig. 1b), making it one of the highest among OHMs. The η_{L-S} , which represents the strength of spin-orbit correlation $\langle \mathbf{L} \cdot \mathbf{S} \rangle$ in 2D-vdW ferromagnets, is also expected to be significantly stronger. To verify this unique characteristic of the Fe₃GaTe₂, we chose the monolayer, bilayer, trilayer, and bulk structures for theoretical calculations, as shown in Fig. 4a. Comprehensive electronic simulations based on density functional theory were then performed to determine their spin-orbit correlation functions (see calculation details in the Methods and Supplementary Note 4). The FM ground state of the Fe₃GaTe₂ was adopted in calculations for all the structures. For the monolayer Fe₃GaTe₂, the magnetic moments are mainly located on the Fe-I ($\sim 2.38 \mu_B$) and Fe-II atoms (~ 1.41

μ_B), with small opposite contributions from Ga ($\sim -0.11 \mu_B$) and Te atoms ($\sim -0.09 \mu_B$) due to hybridization. Similarly, the bilayer, trilayer, and bulk Fe_3GaTe_2 exhibit a nearly identical distribution of magnetic moments as the monolayer Fe_3GaTe_2 , due to the relatively weak vdW interaction between the layers. Further analysis of the orbital resolved band structure reveals that the majority of electronic states near the Fermi level (E_F) are predominantly contributed by the $3d$ orbitals of Fe atoms, as illustrated in Fig. 4b for the monolayer Fe_3GaTe_2 .

The spin-orbit correlation $\langle \mathbf{L} \cdot \mathbf{S} \rangle$ of the FM materials describes the conversion efficiency between the orbital (\mathbf{L}) and the spin (\mathbf{S}). Therefore, we calculated the band-resolved spin-orbit correlation function $\langle \mathbf{L} \cdot \mathbf{S} \rangle_{k,n}$ (9,43) and its integrated value, i.e., spin-orbit correlation coefficient $\eta_{L-S} = \sum_n \int f_{k,n} \langle \mathbf{L} \cdot \mathbf{S} \rangle_{k,n} dV_{k,n}$ after constructing the effective Hamiltonian using the Wannier90 package (44,45) (see Supplementary Note 4), where $f_{k,n} = f(\varepsilon_{k,n})$ represents the Fermi-Dirac distribution of the n th band. The calculated results of $\langle \mathbf{L} \cdot \mathbf{S} \rangle_{k,n}$ are summarized in Figs. 4c-4f, in which red and blue colored areas denote strong positive and negative correlations, respectively. The positive value means that orbital angular momentum is converted to spin angular momentum in the same direction, and vice versa (46). It is evident that positive/negative correlation hotspots appear near the E_F (e.g., around the \mathbf{K} and $\mathbf{K1}$ points) corresponding to strong orbital-to-spin conversion efficiency. Further orbital analysis around these hotspots shows a significant hybridization of the $3d$ orbitals (d_{xy} , $d_{x^2-y^2}$, d_{z^2}), which leads to the large spin-orbit correlation $\langle \mathbf{L} \cdot \mathbf{S} \rangle$. This is because the wave function that consists of d_{xy} and $d_{x^2-y^2}$ gives a larger matrix element's value of

the SOC operator $L \cdot S$ (47). Note that these spin-orbit correlation hotspots occur in only one spin channel, which may further enhance the orbital-to-spin conversion during the OT switching process. Similar correlation hotspots can be observed for bilayer, trilayer, and bulk Fe_3GaTe_2 structures near the E_F (especially near the \mathbf{K} and $\mathbf{K1}$ point), as plotted in Figs. 4d-4f, confirming the robust spin-orbit correlation in Fe_3GaTe_2 .

The spin-orbit correlation coefficient η_{L-S} was calculated to be around 0.375, 0.755, 1.153, and 0.762 for the monolayer, bilayer, trilayer, and bulk Fe_3GaTe_2 structures, respectively. This variation of η_{L-S} is due to the increased energy bands that contribute the $\langle L \cdot S \rangle_{k,n}$ below the E_F as the number of layers increases. Therefore, to compare the effective orbital-to-spin conversion efficiency in the monolayer, bilayer, trilayer, and bulk Fe_3GaTe_2 structures, we defined $\eta_{L-S}^{\text{eff}} = \eta_{L-S}/N$ (N is the number of layers) to assess the spin-orbit correlation of each layer, which was estimated to be around 0.3752, 0.3773, 0.3842, and 0.3809, respectively, almost independent of the layer thickness. It is important to note that the 2D-vdW PMA ferromagnets are fundamentally different from traditional bulk PMA FM material due to their unique 2D-vdW nature. The switching of each magnetic layer could be much easier because of the robust thickness-independent η_{L-S}^{eff} and the rather weak interlayer coupling. These results not only reveal the different orbital-to-spin conversion mechanisms between the 2D-vdW ferromagnets and traditional ferromagnets but also provide insight into understanding the orbital current transport in the ferromagnets with unique 2D-vdW features.

Discussion

To summarize, we investigated the current-induced magnetization switching of the 2D-vdW FM Fe_3GaTe_2 heterostructures using Ti, Pt, and Pt/Ti. We found that the OT from the Ti OHM enables efficient magnetization switching of the 2D-vdW FM Fe_3GaTe_2 at 275 K with the $J_s \sim 2.4 \times 10^6 \text{ A/cm}^2$, compared to the SOT from the Pt ($J_s \sim 9.2 \times 10^6 \text{ A/cm}^2$) and the combined SOT+OT from the Pt/Ti ($J_s \sim 5.9 \times 10^6 \text{ A/cm}^2$). This indicates a highly efficient charge-to-orbital-to-spin current conversion in the 2D-vdW $\text{Fe}_3\text{GaTe}_2/\text{Ti}$ heterostructure. The underlying physical mechanism is that the Ti OHM efficiently converts the charge current into the orbital current due to its high $\sigma_{\text{OHE}} \sim 4600 (\hbar/e)(\text{S/cm})$, while the Fe_3GaTe_2 effectively converts the orbital current into the spin current via a significant and layer-independent $\eta_{\text{L-S}}$, as confirmed by the spin-orbit correlation calculations.

The efficient 2D-vdW orbitronic devices can be realized through the optimal selection of the OHMs and the 2D-vdW ferromagnet to obtain the efficient conversion of charge-to-orbital-to-spin current. Most importantly, investigating the conversion process and transport properties of orbital current in the 2D-vdW FM Fe_3GaTe_2 is crucial for understanding the physical mechanisms behind orbital-to-spin current conversion and magnetization switching in 2D-vdW ferromagnet OT heterostructures. In addition, because of the weak interlayer coupling, 2D-vdW FM materials may lead to much faster magnetization switching of each FM layer. Our experimental and theoretical findings carry important implications for the development of efficient 2D-vdW orbitronic memory and logic devices.

Methods

Crystal growth and property characterizations: High-quality Fe_3GaTe_2 single crystal samples were grown by the self-flux method. Tellurium (Te) powder (99.999%), gallium (Ga) balls (99.9999%), and iron (Fe) powder (99.95%) in a molar ratio of 2:1:2 were sealed in an evacuated quartz tube using a hydrogen-oxygen cutting machine. Subsequently, the quartz tube was heated from room temperature to 1000 °C for 60 minutes in a muffle furnace and maintained at 1000 °C for 1440 minutes, then cooled down from 1000 °C to 780 °C with three-temperature steps. After that, the quartz tube was quenched in the ice-water. The crystalline and magnetic properties of the Fe_3GaTe_2 flakes were characterized by powder X-ray diffraction (XRD), scanning transmission electron microscopy (STEM), physical property measurement system (PPMS), and Vibrating Sample Magnetometer (Model 3107, East Changing Technologies, China).

Device fabrication and transport-property measurements: 2D-vdW FM $\text{Fe}_3\text{GaTe}_2/\text{X}$ (X = Ti, Pt, and Pt/Ti) Hall bar devices were prepared by combining mechanical exfoliation and magnetron sputtering. 2D-vdW FM Fe_3GaTe_2 layers were exfoliated on Si/SiO₂ substrates in an Argon-filled glove box and then transferred into the chamber of the sputtering system with a base pressure lower than 5.0×10^{-8} Torr. After slight surface cleaning, the Ti, Pt, and Pt/Ti layers were deposited on the Fe_3GaTe_2 layer capped with a 3.0-nm-thick SiO₂ layer. During the deposition process, the Ar working pressure is 3.0 mTorr. Subsequently, the $\text{Fe}_3\text{GaTe}_2/\text{Ti}$, $\text{Fe}_3\text{GaTe}_2/\text{Pt/Ti}$,

and Fe₃GaTe₂/Pt samples were patterned into 4-terminal Hall bar devices through the standard photolithography and an Ar ion milling technique.

The anomalous Hall resistance (R_{AHE}) vs. the external magnetic field (H_{ext}) loops of the Fe₃GaTe₂/Ti, Fe₃GaTe₂/Pt/Ti, and Fe₃GaTe₂/Pt Hall bar devices were measured using the Electrical Transport Option of the PPMS Dynacool system. Current-induced magnetization switching experiments were performed with a fixed H_{ext} of ± 20 mT - ± 150 mT along the current direction by interfacing a Keithley 6221 current source and 2182A nanovoltmeter in the Multi-Field Technology Company system.

Theoretical calculation: Bulk vdW FM Fe₃GaTe₂ shares hexagonal lattice structure with space group P6₃/mmc ($a = b = 3.986$ Å, $c = 16.229$ Å, $\alpha = \beta = 90^\circ$, $\gamma = 120^\circ$). In each Fe₃GaTe₂ layer, the Fe₃Ga heterometallic slab is sandwiched between two Te layers, as illustrated in Fig. 1a. To eliminate interactions between slabs along the z direction, we adopted 20 Å vacuum layer along the z -axis. The adjacent slabs were connected by weak vdW forces with an interlayer spacing of 0.81 nm. We performed first-principles calculations based on the density functional theory (DFT) as implemented in the Vienna *ab initio* simulation package (VASP) (48,49), which is treated by the projector-augmented plane-wave (PAW) method and utilized a plane wave basis set (50). The exchange-correlation potential terms were considered at the level of generalized gradient approximation (GGA) within the scheme of Perdew-Burke-Ernzerhof (PBE) functional (51). For few-layer and bulk structures, the long-range vdW interactions [DFT-D3 method (52)] were incorporated to correct its total energy. The plane-wave cutoff energy is chosen as 400 eV, and we sample the

Brillouin zone on $15 \times 15 \times 1$ and $15 \times 15 \times 3$ regular mesh for the self-consistent calculations of few-layer and bulk Fe_3GaTe_2 structures, respectively. The geometric optimizations were performed with a convergence criterion of 10^{-5} eV.

REFERENCES

1. B. Dieny, et al., Opportunities and challenges for spintronics in the microelectronics industry. *Nat. Electron.* 3, 446-459 (2020).
2. Q. Shao, et al., Roadmap of spin-orbit torques. *IEEE Trans. Magn.* 57, 800439 (2021).
3. Z. X. Guo, et al., Spintronics for energy efficient computing: An overview and outlook. *Proc. IEEE* 109, 1398-1417 (2021).
4. A. Brataas, A. D. Kent & H. Ohno, Current-induced torques in magnetic materials. *Nat. Mater.* 11, 372-381 (2012).
5. L. Liu, et al., Spin-torque switching with the giant spin Hall effect of tantalum. *Science* 336, 555-558 (2012).
6. J. Sinova, et al., Spin Hall effects. *Rev. Mod. Phys.* 87, 1213 (2015).
7. C. Song, et al., Spin-orbit torques: Materials, mechanisms, performances, and potential applications. *Prog. Mater. Sci.* 118, 100761 (2021).
8. B. A. Bernevig, T. L. Hughes, and S. C. Zhang, Orbitronics: the intrinsic orbital current in p-doped silicon. *Phys. Rev. Lett.* 95, 066601 (2005).
9. H. Kontani, et al., Giant orbital Hall effect in transition metals: Origin of large spin and anomalous Hall effects. *Phys. Rev. Lett.* 102, 016601 (2009).
10. D. Go, et al., Intrinsic spin and orbital Hall effects from orbital texture. *Phys. Rev. Lett.* 121, 086602 (2018).
11. D. Jo, D. Go, and H.-W. Lee, Gigantic intrinsic orbital Hall effects in weakly spin-orbit coupled metals. *Phys. Rev. B* 98, 214405 (2018).
12. D. Lee, et al., Orbital torque in magnetic bilayers. *Nat. Commun.* 12, 6710 (2021).
13. S. Han, H. W. Lee, and K. W. Kim, Orbital dynamics in centrosymmetric systems. *Phys. Rev. Lett.* 128, 176601 (2022).
14. G. Sala, and P. Gambardella, Giant orbital Hall effect and orbital-to-spin conversion in 3d, 5d, and 4f metallic heterostructures. *Phys. Rev. Res.* 4, 033037 (2022).
15. D. Go, et al., Long-range orbital torque by momentum-space hotspots. *Phys. Rev. Lett.* 130, 246701 (2023).
16. Y. G. Choi, et al., Observation of the orbital Hall effect in a light metal Ti. *Nature* 619, 52-56 (2023).
17. H. Hayashi, et al., Observation of long-range orbital transport and giant orbital torque. *Commun. Phys.* 6, 32 (2023).
18. G. Sala, et al., Orbital Hanle magnetoresistance in a 3d transition metal. *Phys. Rev. Lett.* 131, 156703 (2023)

19. H. Hayashi, D. Go, S. Haku, Y. Mokrousov, and K. Ando, Observation of orbital pumping. *Nat. Electron.* 7, 646-652 (2024)
20. Y. H. Yang, et al., Orbital torque switching in perpendicularly magnetized materials. *Nat. Commun.* 15, 8645 (2024).
21. H. Xie, et al., Efficient noncollinear antiferromagnetic state switching induced by the orbital Hall effect in chromium. *Nano Lett.*, 23, 10274-10281(2023).
22. Z. Zheng, et al., Effective electrical manipulation of a topological antiferromagnet by orbital torques. *Nat. Commun.* 15, 745 (2024).
23. H. Lee, H.-W. Lee, Composition dependence of the orbital torque in $\text{Co}_x\text{Fe}_{1-x}$ and $\text{Ni}_x\text{Fe}_{1-x}$ alloys: Spin-orbit correlation analysis. *Curr. Appl. Phys.* 67, 60-68 (2024).
24. C. Gong, et al., Discovery of intrinsic ferromagnetism in two-dimensional van der Waals crystals. *Nature* 546, 265-269 (2017).
25. B. Huang, et al., Layer-dependent ferromagnetism in a van der Waals crystal down to the monolayer limit. *Nature* 546, 270-273 (2017).
26. X. Lin, et al., Two-dimensional spintronics for low-power electronics. *Nat. Electron.* 2, 274-283 (2019).
27. H. Yang, et al., Two-dimensional materials prospects for non-volatile spintronic memories. *Nature* 606, 663-673 (2022).
28. W. Zhu, et al. Large room-temperature magnetoresistance in van der Waals ferromagnet/semiconductor junctions. *Chin. Phys. Lett.* 39, 128501 (2022).
29. Z.-C. Pan, et al., Room-temperature orbit-transfer torque enabling van der Waals magnetoresistive memories. *Sci. Bull.* 68, 2743-2749 (2023).
30. Z. Li, et al. Room-temperature sub-100 nm Néel-type skyrmions in non-stoichiometric van der Waals ferromagnet $\text{Fe}_{3-x}\text{GaTe}_2$ with ultrafast laser writability. *Nat. Commun.* 15, 1017 (2024).
31. X. Lv, et al., Distinct skyrmion phases at room temperature in two-dimensional ferromagnet Fe_3GaTe_2 . *Nat. Commun.* 15, 3278 (2024).
32. C. Zhang, et al., Above-room-temperature chiral skyrmion lattice and Dzyaloshinskii-Moriya interaction in a van der Waals ferromagnet $\text{Fe}_{3-x}\text{GaTe}_2$. *Nat. Commun.* 15, 4472 (2024).
33. C. Liu, et al., Magnetic skyrmions above room temperature in a van der Waals ferromagnet Fe_3GaTe_2 . *Adv. Mater.* 36, 2311022 (2024).
34. W. H. Li, et al., Room-temperature van der Waals ferromagnet switching by spin-orbit torques. *Adv. Mater.* 35, 2303688 (2023).
35. C. Yun et al., Efficient current-induced spin torques and field-free magnetization switching in a room-temperature van der Waals magnet. *Sci. Adv.* 9, ead3955 (2023).

36. S. N. Kajale, et al., Current-induced switching of a van der Waals ferromagnet at room temperature. *Nat. Commun.* 15, 1485 (2024).
37. G. S. Choi, et al., Highly efficient room-temperature spin-orbit-torque switching in a Van der Waals heterostructure of topological insulator and ferromagnet. *Adv. Sci.* 11, 2400893 (2024).
38. Y. Zhang, et al., Robust field-free switching using large unconventional spin-orbit torque in an all-Van der Waals heterostructure. *Adv. Mater.* 36, 2406464 (2024).
39. S. N. Kajale et al., Field-free deterministic switching of all-van der Waals spin-orbit torque system above room temperature. *Sci. Adv.* 10, eadk8669 (2024).
40. G. Zhang, et al. Above-room-temperature strong intrinsic ferromagnetism in 2D van der Waals Fe_3GaTe_2 with large perpendicular magnetic anisotropy. *Nat. Commun.* 13, 1-8 (2022).
41. S. L. Ding, et al., Harnessing orbital-to-spin conversion of interfacial orbital currents for efficient spin-orbit torques. *Phys. Rev. Lett.* 125, 177201 (2020).
42. S. Lee, et al., Efficient conversion of orbital Hall current to spin current for spin-orbit torque switching. *Commun. Phys.* 4, 234 (2021).
43. T. Tanaka, et al. Intrinsic spin Hall effect and orbital Hall effect in 4d and 5d transition metals. *Phys. Rev. B* 77, 165117 (2008).
44. I. Souza, N. Marzari, and D. Vanderbilt, Maximally localized Wannier functions for entangled energy bands, *Phys. Rev. B* 65, 035109 (2001).
45. N. Marzari and D. Vanderbilt, Maximally localized generalized Wannier functions for composite energy bands, *Phys. Rev. B* 56, 12847 (1997).
46. M. Schreier, et al. Sign of inverse spin Hall voltages generated by ferromagnetic resonance and temperature gradients in yttrium iron garnet platinum bilayers. *J. Phys. D: Appl. Phys.* 48, 025001 (2015).
47. S. Konschuh, M. Gmitra, and J. Fabian, Tight-binding theory of the spin-orbit coupling in grapheme. *Phys. Rev. B* 82, 245412 (2010).
48. G. Kresse and J. Furthmüller, Efficiency of ab-initio total energy calculations for metals and semiconductors using a plane-wave basis set, *Comput. Mater. Sci.* 6, 15 (1996).
49. G. Kresse and J. Hafner, Ab initio molecular-dynamics simulation of the liquid-metal-amorphous-semiconductor transition in Germanium, *Phys. Rev. B* 49, 14251 (1994).
50. P. E. Blöchl, Projector augmented-wave method, *Phys. Rev. B* 50, 17953 (1994).
51. J. P. Perdew, et al., Atoms, molecules, solids, and surfaces: Applications of the generalized gradient approximation for exchange and correlation, *Phys. Rev. B* 46, 6671 (1992).

52. S. Grimme, Semiempirical GGA-type density functional constructed with a long-range dispersion correction, *J. Comput. Chem.* 27, 1787 (2006).

Acknowledgments: This work was supported by the National Key R&D Program of China (2022YFA1204003), the National Natural Science Foundation of China (Grant Nos. 52271240, U23A20551, 12204037) and the Key project of the Natural Science Foundation of Tianjin (Grant No. 23JCZDJC00400). D.L.Z gratefully acknowledges the research funding provided by the Cangzhou Institute of Tiangong University (Grant No. TGCYY-F-0201) and the Key R&D Program of Cangzhou (222104008). We would like to thank the Analytical & Testing Center of Tiangong University.

Author contributions: D.L.Z., H.S.W., J.Y.D., and J.L.C. contributed equally to this work. D.L.Z conceived the work and designed all the samples. Y.J. coordinated and supervised the project. H.S.W., and J.Y.D. prepared the samples and patterned the Hall bar devices with the help by Y.H.Y. and J.L.G.. J.Y.D. and H.S.W. carried out the current-induced orbital/spin-torque magnetization switching experiments with the help P.W., S.H., and Z.Y.J.. J.L.C., and W.J. performed the first-principles calculations. D.D.Y., J.X.Y., and K.Z. prepared the Fe₃GaTe₂ single crystals and characterized the crystalline structure and magnetic properties. W.H.W. and Y.L. help analyze the experimental data. D.L.Z. and W.J. wrote the manuscript with inputs from all the authors. All the authors discussed the results and commented on the manuscript.

Competing interests: Authors declare no competing interests.

Data availability: All data are available in the manuscript or the Supplementary Materials.

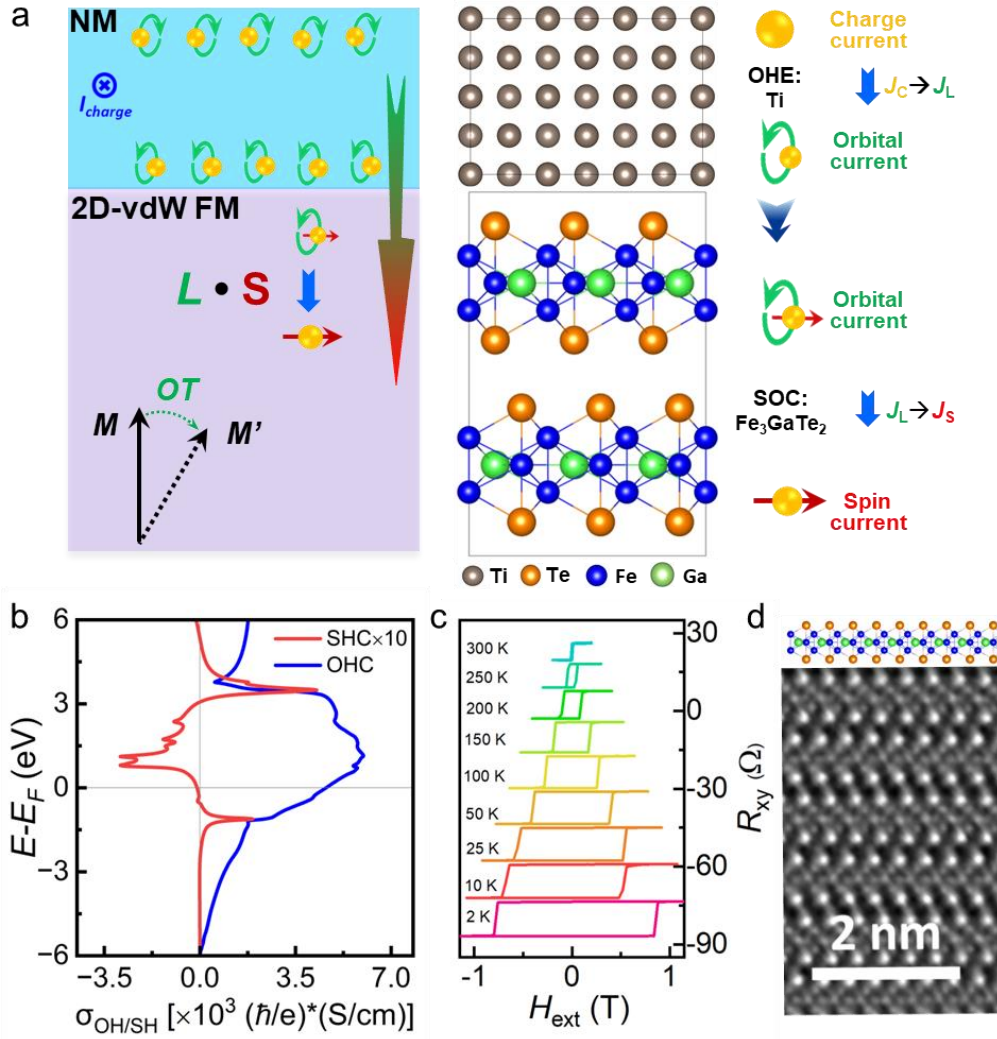


Fig. 1. Orbital torque in van der Waals ferromagnet. **a.** Schematic of the $\text{Fe}_3\text{GaTe}_2/\text{Ti}$ orbital torque heterostructure, in which the Ti orbital Hall material converts the charge current (J_C) into the orbital current (J_L), then the orbital current (J_L) flows into the 2D-vdW FM Fe_3GaTe_2 layer and is converted into the spin current (J_S) due to the spin-orbital coupling of the Fe_3GaTe_2 layer. **b.** The calculated orbital Hall conductivity (blue line) and spin Hall conductivity (red line) of the Ti orbital Hall material. **c.** The anomalous Hall resistance (R_{xy}) vs. out-of-plane magnetic field H_{ext} as a function of the temperature of the Fe_3GaTe_2 nanoflake. **d.** The atomic-resolution HAADF-TEM image of the Fe_3GaTe_2 single crystal.

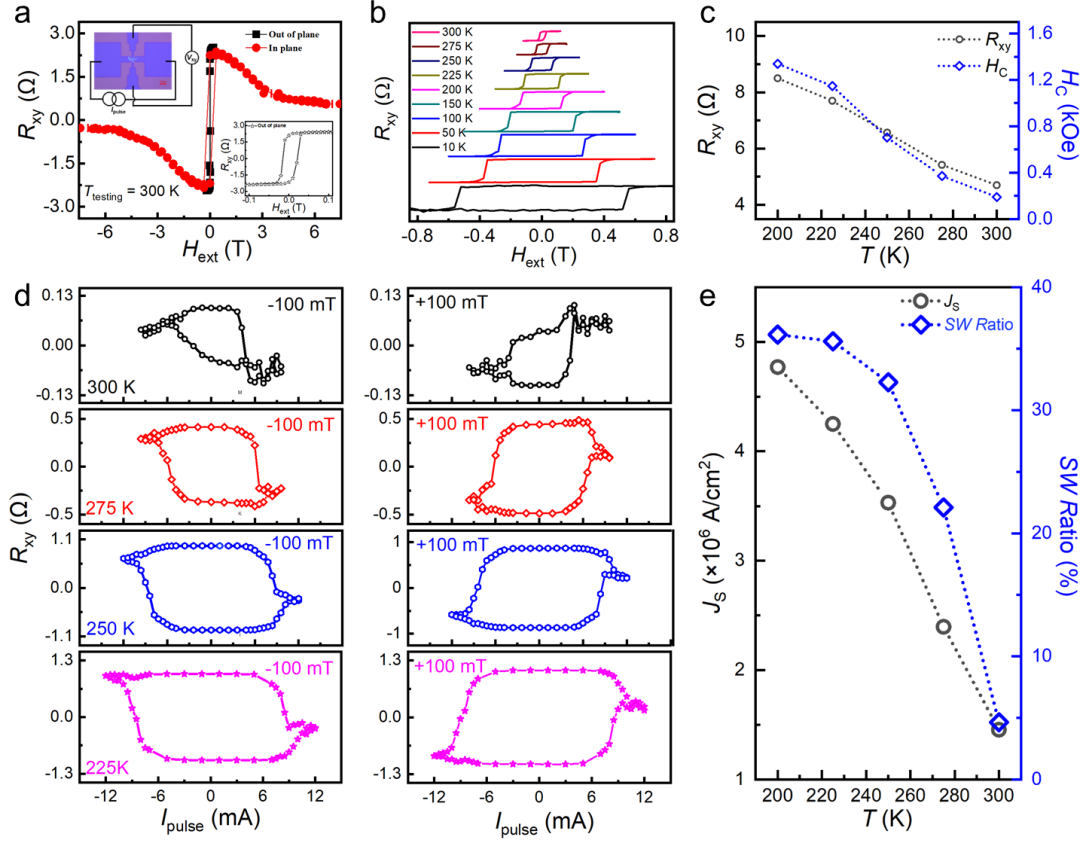


Fig. 2. Orbital torque switching of 2D vdW ferromagnet. **a.** The anomalous Hall resistance (R_{AHE}) vs. the external magnetic field (H_{ext}) loops measured at room temperature of the 2D-vdW $\text{Fe}_3\text{GaTe}_2/\text{Ti}$ Hall bar device, where the H_{ext} is applied along in-plane and out-of-plane directions. The insets show the image of the Hall bar device and the zoom-in out-of-plane R_{AHE} vs. H_{ext} loop. **b.** The R_{AHE} vs. H_{ext} loops as a function of measuring temperatures of the $\text{Fe}_3\text{GaTe}_2/\text{Ti}$ device. **c.** The curves of the R_{AHE} vs. T_{testing} and the coercivity (H_C) vs. T_{testing} of the $\text{Fe}_3\text{GaTe}_2/\text{Ti}$ Hall bar device. **d.** The R_{AHE} vs. the pulse current (I_{pulse}) loops of the $\text{Fe}_3\text{GaTe}_2/\text{Ti}$ device measured with the in-plane $H_{\text{ext}} = \pm 100$ mT along the current direction at temperatures from 300 K to 225 K. **e.** The J_S vs. T_{testing} , and the switching ratio vs. T of the $\text{Fe}_3\text{GaTe}_2/\text{Ti}$ device.

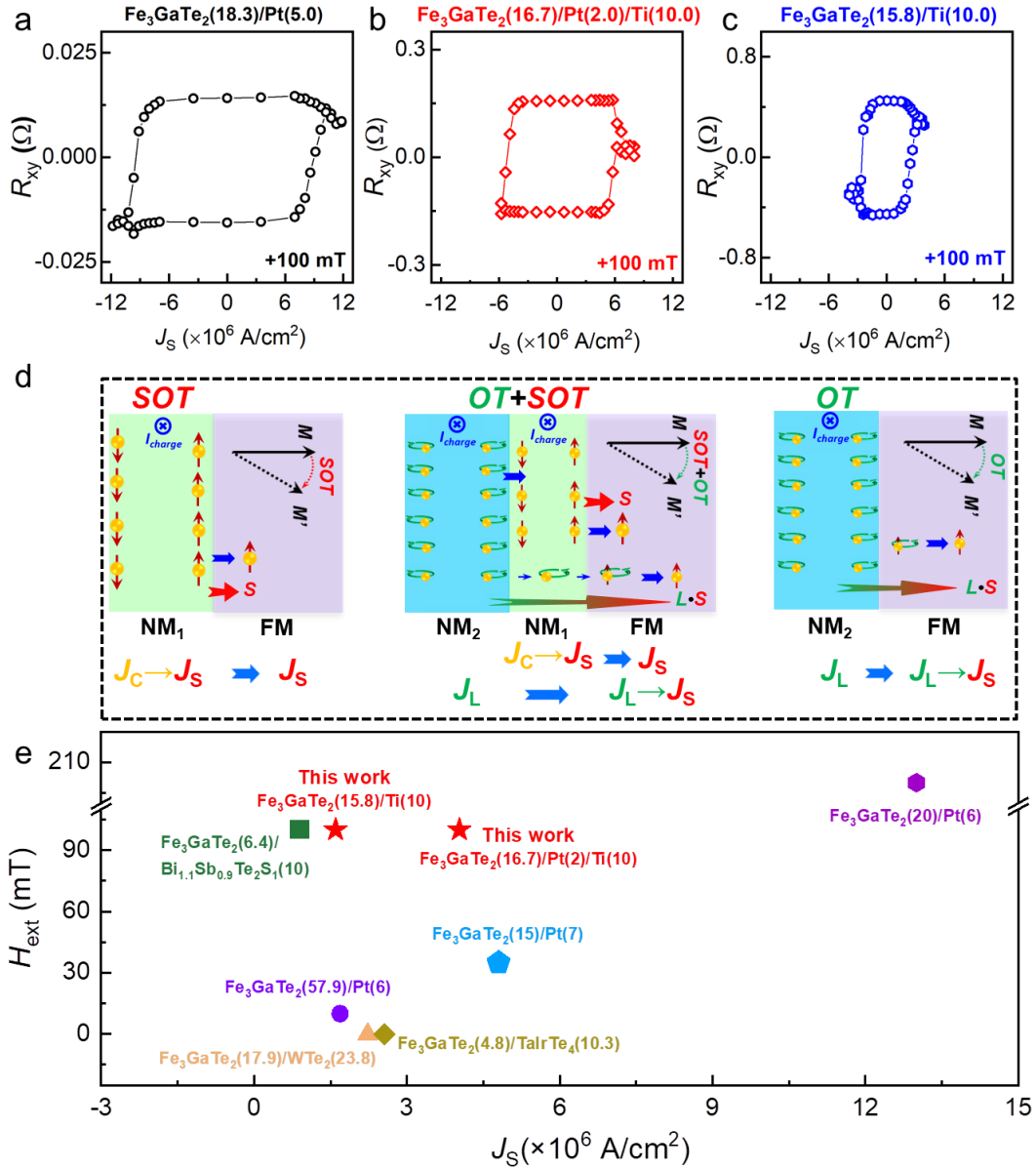


Fig. 3. Orbital torque vs. Spin-orbit torque. **a-c.** The anomalous Hall resistance (R_{AHE}) vs. the switching current density (J_S) loops measured at 275 K of the 2D-vdW $\text{Fe}_3\text{GaTe}_2/\text{Pt}$, $\text{Fe}_3\text{GaTe}_2/\text{Pt}/\text{Ti}$, and $\text{Fe}_3\text{GaTe}_2/\text{Ti}$ Hall bar devices, respectively, under the in-plane external magnetic field ($H_{\text{ext}} = 100$ mT) along the current direction. **d.** The physical mechanisms of the current conversion for the SOT, SOT+OT, and OT devices. **e.** The summarized J_S values as a function of the in-plane H_{ext} for 2D-vdW Fe_3GaTe_2 heterostructures driven through the SOT and OT at room temperature.

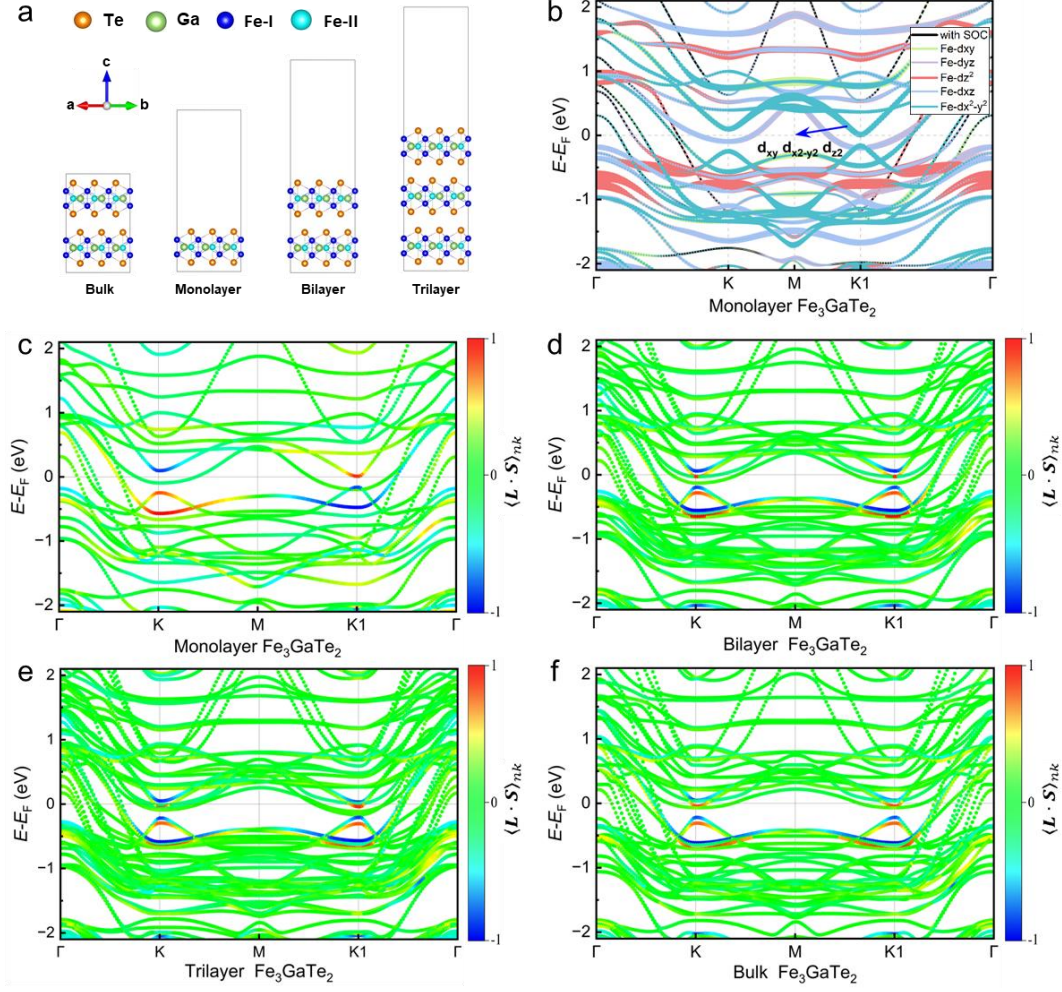


Fig. 4. Theoretical calculation of spin-orbit correlation function $\langle L \cdot S \rangle_{nk}$. **a.** The monolayer, bilayer, trilayer, and bulk Fe_3GaTe_2 structures, in which the Fe-I, Fe-II, Ga, and Te atoms are colored blue, light blue, green, and orange, respectively. **b.** The orbital-projected band structure of monolayer Fe_3GaTe_2 structure with different d states of Fe is highlighted by different colors. **c-f.** The calculated band-resolved spin-orbit correlation function $\langle L \cdot S \rangle_{nk}$ of the monolayer, bilayer, trilayer, and bulk Fe_3GaTe_2 structures, respectively. The color represents the correlation for each eigenstate, in which red and blue denote strong positive and negative correlations, respectively. Note that the Fermi energy is set to zero for reference.